www.sciencemag.org/cgi/content/full/340/6131/460/DC1

Supplementary Materials for

Observations of Ejecta Clouds Produced by Impacts onto Saturn's Rings

Matthew S. Tiscareno,* Colin J. Mitchell, Carl D. Murray, Daiana Di Nino, Matthew M. Hedman, Jürgen Schmidt, Joseph A. Burns, Jeffrey N. Cuzzi, Carolyn C. Porco, Kevin Beurle, Michael W. Evans

*Corresponding author. E-mail: matthewt@astro.cornell.edu

Published 26 April 2013, *Science* **340**, 460 (2013)
DOI: 10.1126/science.1233524

This PDF file includes:

Supplementary Text
Figs. S1 to S11
Tables S1 to S7
References (*25*–*38*)

1 Observations

1.1 Saturnian equinox, 2009

Between one day before and three days after the 2009 equinox event (while the sub-solar latitude was less than $0.05°$, or roughly two solar radii at Saturn), Cassini's Imaging Science Subsystem (ISS) imaged one sheared ejecta cloud in the C ring ($\sim$81,600 km from Saturn center; denoted as apparition "Cx"), a larger one in the B ring ($\sim$114,700 km from Saturn center; apparition "Bx"), and an even larger one on two different occasions in the A ring ($\sim$129,400 km from Saturn center; apparitions "Ax(1)" and "Ax(2)"). The latter structure extended $\sim$300 km radially and more than 5,000 km azimuthally. On each occasion, the structure was seen in multiple images (Table S1), as images with various exposure durations were taken of each footprint due to uncertainty before this unique event as to what the photometric properties of the rings would be. As it happened, the longest exposures invariably gave the best views with the highest signal-to-noise. The brightnesses of these features, relative to the background in terms[1] of I/F, are listed in Table S3.

1.2 High-phase high-resolution images, 2005

Images at very high phase angle ($\alpha \gtrsim 165°$) are only possible when Cassini passes through the planet's shadow, as the safety of its optical instruments would be jeopardized by pointing them so close to the Sun's direction at any other time. Cassini has twice obtained high-resolution images of the rings during such eclipse maneuvers, on 2005 May 3 (DOY 123) and again on 2012 July 22 (DOY 204).

The four images obtained with this geometry in 2005 (Table S1) were centered on the mid-C ring, $\sim$84,000 km from Saturn center, just inward of the Maxwell Gap. The ring region in view (Figure S1) contains the "plateaux" designated P5, P6, and P7, and the embedded ringlets

---

[1] I/F is a measure of observed brightness normalized by the incident solar flux.

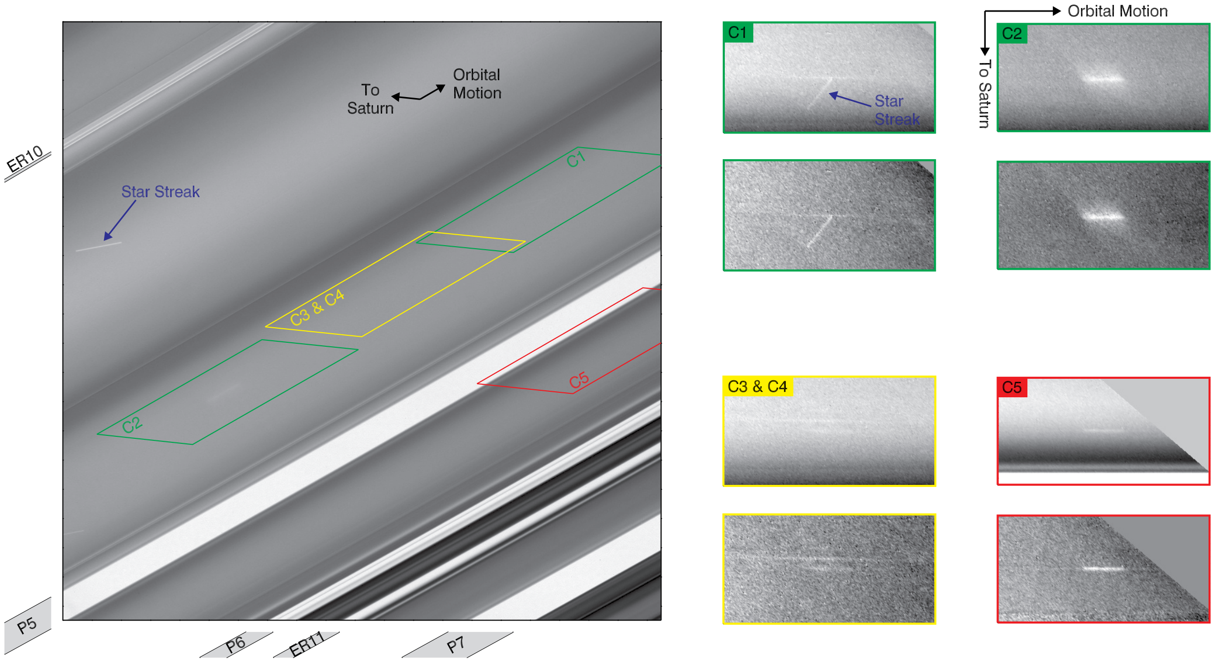

Figure S1: Images obtained during the 2005 eclipse observations, showing features interpreted as ejecta clouds. At left is the entirety of N1493791286, which is very similar in general appearance to the other two images in which features were also seen (see Tables S2 and S3). Along the bottom and left edges of the full image are labels indicating well-known C ring landmarks, including plateaux ("P") and embedded ringlets ("ER"), as tabulated by (*19*). At right are four pairs of reprojected portions of images N1493791286 (green, containing streaks "C1" and "C2"), N1493791602 (yellow, containing streaks "C3" and "C4"), and N1493792122 (red, containing streak "C5"), the footprints of which are shown in the full image. In each pair of reprojections, the top panel shows the image unprocessed except for a brightness stretch, while the bottom panel shows the image after an average radial profile has been removed. The five observed streaks trend in the direction of orbital motion because of smearing during the exposure, though streaks "C1," "C3," and "C4" are longer due to keplerian shear. Several star streaks are also visible, oriented at a different angle determined by the spacecraft's motion; two examples are labeled in blue, including one that nearly intersects streak "C1."

designated ER10, ER11, and ER12 (*19*). These four images contained five short azimuthal lines (designated "C1" through "C5"), three quite faint, one about three times as bright and another about 30 times as bright (see Table S3). We will assume that the frequency of such features (five in four images) is typical for images at this phase and resolution.

At this location, orbital velocity is $\sim$21 km s^{-1}, so a bright point source in the ring will trace out a $\sim$200-km stream during the 10-second exposures. So, in contrast to the features described in Section 1.1, whose morphology is primarily determined by *shear*, in this case the morphology is determined by *smear*. The structures causing the observed features are likely clouds of dust, as they seem ubiquitous in these very-high-phase high-resolution images but have not been seen in lower-phase images at similar resolution. The two brightest features ("C2" and "C5") both have streaks of length[2] 200 km, within measurement error (Table S2), and have a parallelogram geometry (most easily seen for "C2" in Figure S1) that is to be expected from a canted cloud that has been azimuthally smeared by motion through the field of view during the exposure. The three dimmer features ("C1," "C3," and "C4"), on the other hand, have little discernible radial structure but are longer than expected from keplerian smear alone (Table S2), probably

---

[2] The *apparent* lengths of C2 and C5 are 165 km, agreeing with each other within measurement error, but our measurements used the spacecraft's position and pointing direction at the midpoint time of the exposure. When we carefully solved for the ring coordinates of the two ends of C2 (the brightest streak, and thus the easiest to work with), respectively at the start time and end time of the exposure, thus accounting for the difference in the spacecraft's position as well as the corresponding difference in its pointing direction between the two times, we found a length of 201.0 km. This is in excellent agreement with the product of the keplerian velocity and the exposure duration. Consequently, the streak lengths reported in Table S2 all reflect the measured apparent lengths plus a constant offset of 35 km.

Table S1: Observing information for images used in this paper.

Image	Orbit	Date/Time	Incidence Angle[a]	Emission Angle[a]	Phase Angle	Radial Resolution[b]	Azimuthal Resolution[b]	Exposure Duration[c]	Name[d]
N1493791286	007	2005-123 05:34:14	111.82°	71.3°	174.3°	4.2	2.7	10.0	C1, C2
N1493791602	007	2005-123 05:39:30	111.82°	71.3°	173.6°	4.1	2.7	10.0	C3, C4
N1493792122	007	2005-123 05:48:10	111.82°	71.2°	172.4°	4.3	2.8	10.0	C5
N1493792962	007	2005-123 06:02:10	111.82°	71.3°	170.4°	4.4	2.8	10.0	
N1628592706	116	2009-222 10:09:37	90.01°	94.6°	150.6°	7.9	50.9	1.0	Bx
N1628592766	116	2009-222 10:10:37	90.01°	94.6°	150.6°	6.9	50.8	0.7	
N1628592826	116	2009-222 10:11:38	90.01°	94.6°	150.6°	6.1	50.8	0.5	
N1628669064	116	2009-223 07:22:15	90.00°	111.7°	149.6°	1.5	4.1	0.7	
N1628669124	116	2009-223 07:23:15	90.00°	111.7°	149.5°	1.5	4.0	1.2	
N1628669191	116	2009-223 07:24:21	90.00°	111.7°	149.3°	1.5	4.0	2.6	Cx
N1628845250	116	2009-225 08:18:40	89.96°	70.0°	90.8°	16.3	8.4	0.8	
N1628845283	116	2009-225 08:19:12	89.96°	70.0°	90.8°	16.3	8.4	1.5	Ax(1)
N1628933401	116	2009-226 08:47:47	89.95°	73.6°	100.3°	9.9	32.8	6.8	Ax(2)
N1628933453	116	2009-226 08:48:40	89.95°	73.6°	100.3°	9.9	32.8	3.8	
N1721654859	169	2012-204 12:35:09	74.85°	102.2°	174.8°	7.7	3.6	2.0	C6
N1721654965	169	2012-204 12:36:55	74.85°	102.2°	174.6°	7.9	3.6	2.0	C6

[a] Measured from the direction of Saturn's north pole (ring-plane normal), so that angles $> 90°$ denote the southern hemisphere.

[b] In km/pixel.

[c] In seconds.

[d] Each equinox feature appears in multiple images, but only that with the longest exposure is used for the further analysis in Tables S2 and S3. The exception is "C6," the two images of which were taken through different color filters, and thus give spectral information.

because their cant angles are small and thus the spreading of the clouds due to keplerian shear is simply added to the smear. We use this inference to estimate the cant angles in Section 2.

1.3 High-phase high-resolution images, 2012

The very-high-phase observations obtained in 2012 (Table S1), intended to follow up on the 2005 and 2009 detections, comprised 12 images centered on the mid-C ring and 11 images centered on the mid-A ring. Like the 2005 images, they view the unlit face of the rings. Only one feature (in the C ring at ∼83,200 km from Saturn center; designated "C6") was detected. The embedded ringlet designated ER10 (*19*) can be seen along the bottom of the image of "C6" shown in Figure 1. Also visible in the bottom-right corner of that image portion is Saturn's shadow falling on the rings, which is to be expected given the very high phase angle.

The 2012 images were taken with rotating color filters (see (*12*)), for the purpose of obtaining spectral information on any detected features, and "C6" was detected in both the Blue filter (BL1/CL2) and an Infrared filter (CL1/IR3). The exposures were short enough that there is no discernible smear.

2 Data Reduction

All images were calibrated and converted to values of the scaled brightness I/F using the standard Cisscal package v3.6 (*12*). The images were navigated using stars and ring edges as fiducials. Relevant portions of each image were then reprojected onto a radius-longitude grid (Figures S2 and S3) using bilinear interpolation and oversampled by a factor of 2. In some cases, underlying radial brightness structure was removed by subtracting an average radial profile constructed from portions of the image adjacent to, but not including, the feature of interest. Then, for each line and sample of the reprojected image, we calculated the integrated brightness, the brightness-weighted center location, and the brightness-weighted gaussian width

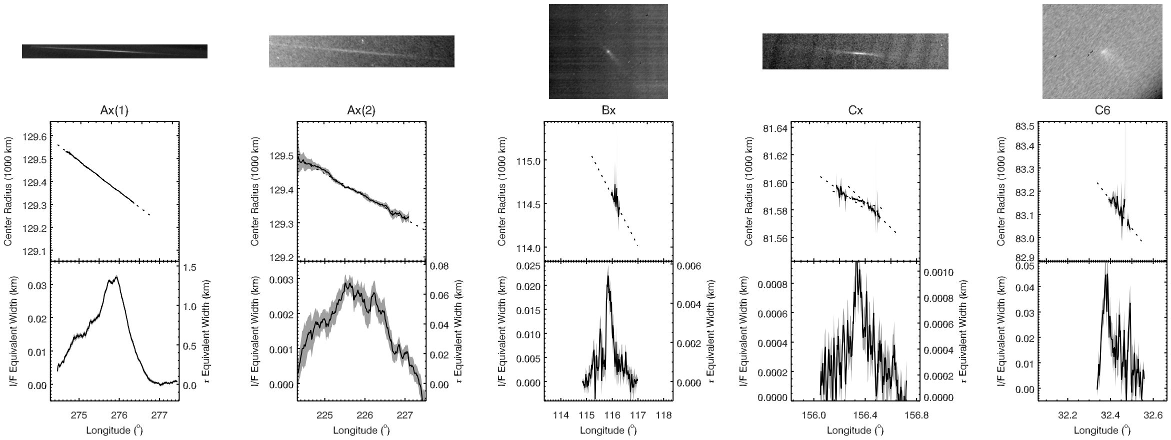

Figure S2: In the top row, images of the non-smeared ejecta clouds are reprojected onto a radius-longitude grid (isotropic in pixel size, not in linear scale). In the subsequent rows are plotted their center radii and equivalent widths, both as a function of longitude. The equivalent width profile for each feature is further summed to obtain the equivalent area, a measure of the feature's total integrated brightness or optical depth (see Section 2). The range of the horizontal axis for all plots, and of the vertical axis in the center radius plots, corresponds to the range of longitudes and radii in the reprojected images. For feature "Cx," slopes were fit separately to the left, center, and right portions of the cloud (see Section 6 and Table S2).

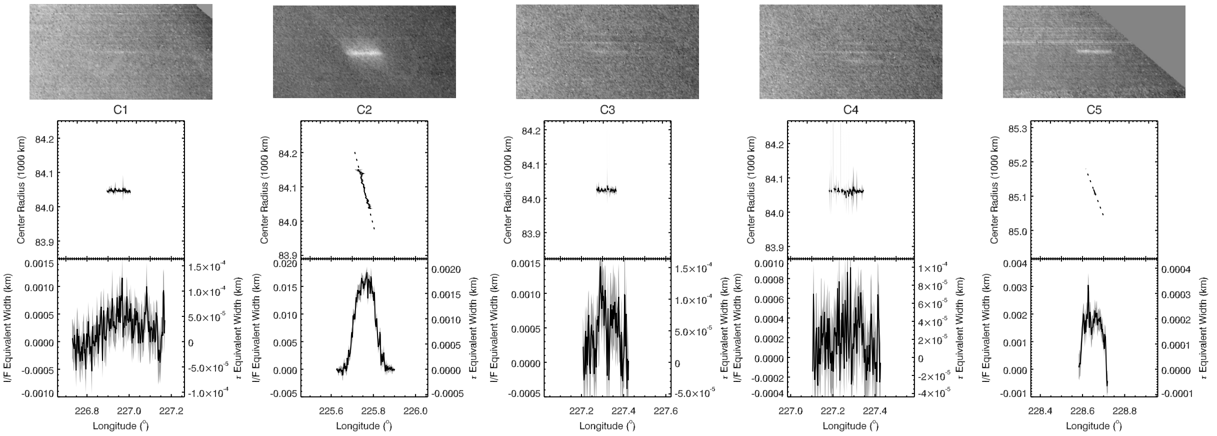

Figure S3: Same as Figure S2, but for the smeared ejecta clouds. For the higher-signal features "C2" and "C5," the center longitude was calculated as a function of radius, in order to estimate the cant angle while averaging over the smearing (see Section 2).

(plotted in Figures S2 and S3).

Using the calculated locations of the feature within the image, Table S2 gives each feature's

Table S2: Fitted spatial parameters for the observed ejecta clouds. For each apparition, only the image with the best signal-to-noise is used (cf. Table S1). The pixel positions and radius and longitude are the position of the geometric center of the structure, not necessarily the center of light. For feature "Cx," slopes were fit separately to the left, center, and right portions of the cloud (see Section 6 and Figure S2).

Name[a]	Image	[line, sample]	Radius[b]	Longitude	Length[b,c]	Orientation[d,e]	Apparent Age (hr)	Region
C1	N1493791286	[313, 811]	84046	226.93°	295	$\sim 4°$	~ 10	
C2	”	[632, 282]	84085	225.76°	200	$59° \pm 1°$	0.44 ± 0.02	
C3	N1493791602	[446, 565]	84022	227.33°	215	$\sim 40°$	~ 1	
C4	”	[467, 548]	84061	227.26°	280	$\sim 7°$	~ 6	
C5	N1493792122	[515, 950]	85117	228.65°	200	$48° \pm 2°$	0.67 ± 0.04	
Bx	N1628592706	[716, 567]	114685	115.83°	1100	$16° \pm 1°$	4.1 ± 0.4	
Cx	N1628669191	[860, 589]	81582	156.37°	860	$1.3° \pm 0.1°$	30 ± 3	Central
						$2.7° \pm 0.4°$	15 ± 2	Left
						$3.6° \pm 0.3°$	10.9 ± 0.8	Right
Ax(1)	N1628845283	[374, 373]	129380	275.80°	4900	$3.396° \pm 0.005°$	23.52 ± 0.03	
Ax(2)	N1628933401	[168, 521]	129384	225.91°	6200	$1.68° \pm 0.01°$	47.6 ± 0.4	
C6	N1721654965	[569, 207]	83196	32.37°	200	$40° \pm 2°$	0.86 ± 0.05	

[a] See Section 1 for format.

[b] In km.

[c] For the smeared features "C1" through "C5," we have added 35 km to the apparent length, which we calculated for a single geometrical solution referenced to the midpoint time of the exposure. The extra 35 km arise when accounting for the difference in the spacecraft's position, and the corresponding difference in its pointing direction, between the beginning and the end of the exposure (see Section 2).

[d] Relative to a line of constant radius.

[e] For high-signal smeared ejecta clouds "C2" and "C5," centers of brightness were measured in the azimuthal direction to neutralize the smear, and calculation of the orientation proceeded. For low-signal smeared ejecta clouds "C1," "C3," and "C4," the orientation was estimated by dividing the feature's radial width by its azimuthal length (less the smear length), then taking the arctangent of that quotient.

Table S3: Fitted brightness parameters for observed ejecta clouds. For each apparition, only the image with the best signal-to-noise is used (cf. Table S1) with the exception of "C6," for which the two images were taken with different filters and thus each give useful spectral information.

Name[a]	Image	[line, sample]	Peak I/F	Peak τ[c]	Equivalent Area[b,c]	Spectral Filter
C1	N1493791286	[313, 811]	0.0001	0.00002	0.015 ± 0.002	Clear (CL1/CL2)
C2	”	[632, 282]	0.0004	0.00004	0.340 ± 0.004	Clear (CL1/CL2)
C3	N1493791602	[446, 565]	0.0001	0.00001	0.014 ± 0.002	Clear (CL1/CL2)
C4	”	[467, 548]	0.0002	0.00002	0.009 ± 0.001	Clear (CL1/CL2)
C5	N1493792122	[515, 950]	0.0002	0.00003	0.037 ± 0.001	Clear (CL1/CL2)
Bx	N1628592706	[716, 567]	0.0005	0.0001	4.6 ± 0.2	Clear (CL1/CL2)
Cx	N1628669191	[860, 589]	0.0002	0.0002	0.32 ± 0.01	Clear (CL1/CL2)
Ax(1)	N1628845283	[374, 373]	0.0007	0.03	3643 ± 5	Clear (CL1/CL2)
Ax(2)	N1628933401	[168, 521]	0.00008	0.002	267 ± 3	Clear (CL1/CL2)
C6	N1721654859	[10, 270]	0.0009	0.00006	0.18 ± 0.01	Blue (BL1/CL2)
C6	N1721654965	[569, 207]	0.001	0.00008	0.35 ± 0.02	Infrared (CL1/IR3)

[a] See Section 1 for format.

[b] Calculated in terms of optical depth τ, with units km^2.

[c] Inferred optical depths for events "Ax(1)" and "Ax(2)" are sensitive to the ejecta particle-size distribution, which is not independently known (see Section 2 and Figure S4). For $q \neq 3$, the tabulated "Peak τ" and "Equivalent Area" should be multipled by factors given in Table S4.

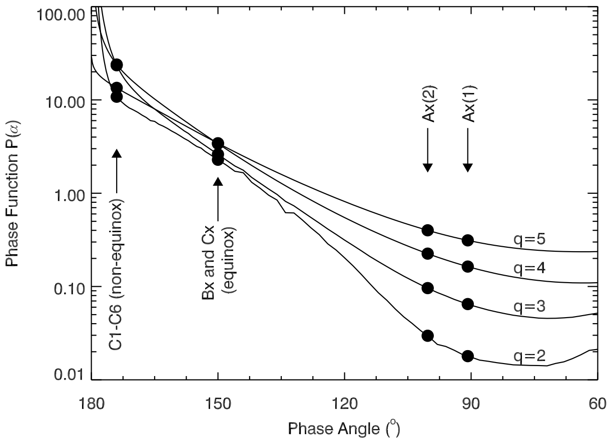

Figure S4: Calculations of the phase function $P(\alpha)$ using Mie theory (*25*) as a function of phase angle. Curves are shown for size-distribution power-law index q ranging from 2 to 5. An upper size cutoff of 0.4 mm was used for all phase curves. Also shown on the plot with arrows, and with plotted circles at their intersections with the phase curves, are the phase angles for observations described in this work (see Tables S1 and S3).

position in terms of line and sample (i.e., pixel position within the image) as well as in terms of radius and longitude within Saturn's equatorial plane. The length of the feature is given in km.

We discuss the relation of cant angle to the apparent age of the feature in Section 3. For the non-smeared features, the cant angle is determined by simply fitting a line to the brightness-weighted center locations and comparing that line to one of constant radius. For the features detected in 2005, we had to compensate for the effects of smearing due to motion of the feature during the image exposure. The two brightest features ("C2" and "C5") are well-enough resolved that we could calculate the center locations in the direction orthogonal to the smear-

Table S4: Factors by which "Peak τ" and "Equivalent Area" from Table S3 should be multiplied to account for changes in the phase function $P(\alpha)$ with the size-distribution power-law index q (see Figure S4).

q	C1–C6	Bx,Cx	Ax(1)	Ax(2)
2	2.175	1.142	3.614	3.242
3	1.000	1.000	1.000	1.000
4	0.983	0.768	0.396	0.427
5	1.748	0.760	0.208	0.240

ing, and then proceed to calculate the cant angle as for the non-smeared features. For the three dimmer features ("C1," "C3," and "C4"), we estimated the cant angle by dividing the radial width by the azimuthal length (with the smear length subtracted from the latter), then taking the arctangent of the quotient.

For the feature seen in the C ring during the 2009 equinox (denoted "Cx," see Figures 1 and S2), the peripheral regions of the cloud have a steeper cant angle than does the bright central region (see Table S2 and Figure S9). We fit the three regions to three separate cant angles and discuss the implications in Section 6.

Table S3 gives the peak brightness (I/F), the peak optical depth τ, and the equivalent area for each feature. Optical depth is derived from I/F using (*26*)

$$\tau = \frac{4\mu I/F}{\varpi_0 P(\alpha)}, \tag{S1}$$

Given the large uncertainties regarding the character and size distribution of particles in the observed clouds, we use a single-scattering albedo $\varpi_0 \sim 0.5$ and we estimate the phase function $P(\alpha)$ from a series of calculations of Mie scattering functions[3] (*25*), shown in Figure S4. The path-length coefficient μ is the sine of the observer's elevation angle (or, equivalently, the cosine of the emission angle; see Table S1), though this has different interpretations depending on the cloud's dimensions: if the cloud is vertically thin, then μ accounts for the path length through the cloud, but if the cloud's vertical height is comparable to its width, then μ accounts for projection of the image onto the ring plane during the calculation of the equivalent area.

The "equivalent area" A is calculated by integrating the cloud's magnitude over its area, in units of the brightness I/F or of the optical depth τ (we will denote the former as $A^{I/F}$ and the latter as A^{τ} when a distinction is needed). This quantity is an extension of the concept of the equivalent width, defined by (*27*) for quantifying azimuthal features in a radially-unresolved ring, but we integrate over two dimensions instead of one (cf. (*28*)) to obtain the total integrated

---

[3] We thank M. R. Showalter for providing this software.

brightness of a compact cloud. In practice we calculate the equivalent width for each row or column of pixels, then integrate the latter into the equivalent area (see the bottom rows of Figures S2 and S3). The equivalent area gives a measure of the total amount of light-scattering material in the cloud, whether it is spread out physically (as for the 2009 data) or by smear (as for the 2005 data), and can be thought of as the area the cloud would cover if its I/F or τ (respectively) were uniformly unity.

3 Cant angle and inferred age

A simple-minded relationship between the cant angle and the time elapsed since the cloud's formation can be obtained from the classic equation for *keplerian shear*, which itself is obtained by differentiating Kepler's Third Law. For mean motion Ω and semimajor axis a,

$$\frac{\mathrm{d}\Omega}{\mathrm{d}a} = -\frac{3}{2}\frac{\Omega}{a}. \tag{S2}$$

If one assumes an initially circular cloud centered on the impact site, containing particles on circular orbits such that radial position r equates with semimajor axis a and changes in the longitudinal position $\Delta\lambda$ are due to changes in the mean motion accumulating with time, $(\Delta\Omega)t$. We denote the cant angle (measured clockwise from a purely azimuthal line) for this case as θ_1 and express it as

$$\tan\theta_1 = \frac{\Delta r}{a\Delta\lambda} = \frac{\Delta a}{a\Delta\Omega t}. \tag{S3}$$

Applying Equation S2, we have

$$\tan\theta_1 = \frac{2}{3\Omega t} = \frac{P}{3\pi t}, \tag{S4}$$

where $P = 2\pi/\Omega$ is the orbital period. A non-circular shape for the initial cloud, such as is discussed in Section 5, becomes unimportant once the cotangent of the cant angle becomes

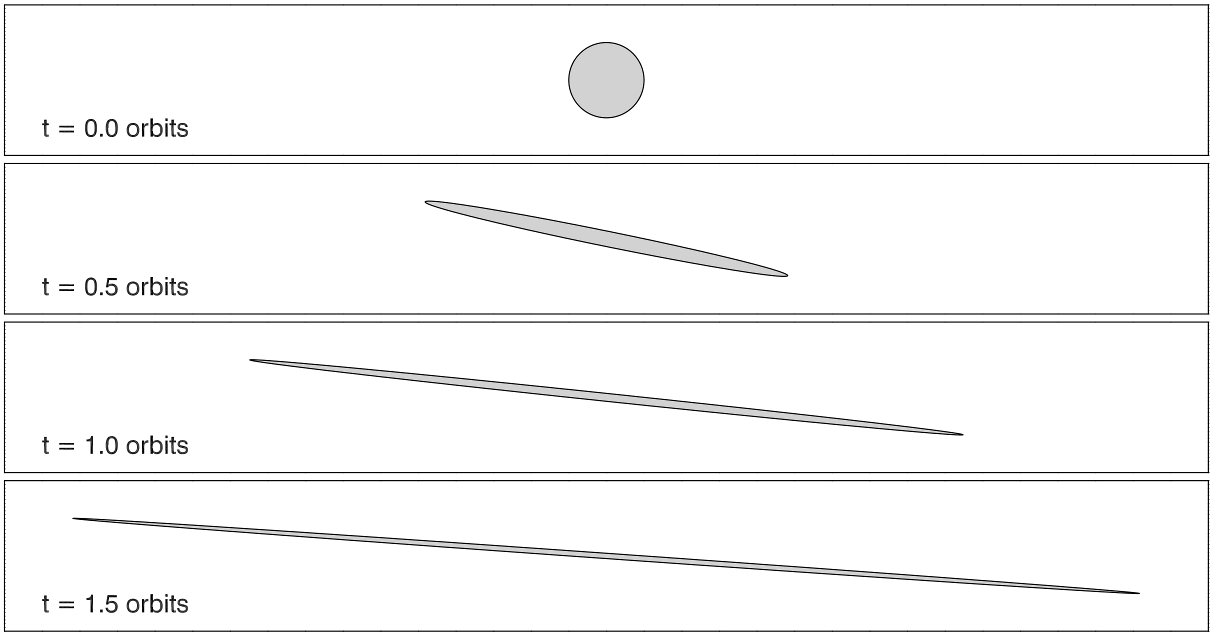

Figure S5: Illustration of the keplerian shear of an initially circular cloud. The time given at the bottom-left of each panel is the number of orbits elapsed, t/P (see Equation S4).

much larger than the aspect ratio of the initial cloud. This process is illustrated in Figure S5 and represented by the dashed line in Figure S6a and the solid line in Figure S7a (cf. Figure 3).

However, impact ejecta clouds do not usually conform to the description given above. Rather, they emanate from a single point (the impact site) with a range of velocities and thus a range of semimajor axes, eccentricities, and inclinations. In particular, the azimuthal component[4] of the ejecta velocity will change the semimajor axis of the ejecta particle by Δa, also giving it an eccentricity $e \sim |\Delta a|/a$ so that its periapse or apoapse remains at the impact site's semimajor axis a. Because of this eccentricity, and because the periapse direction of the ejecta particles at any particular Δa are more or less aligned with each other, the ejecta particles will undergo a coherent epicyclic motion. Adding this epicyclic motion to both the numerator and

---

[4] The radial and vertical components of the ejecta velocity will give the ejecta particles a distribution of orbital elements, thus affecting the second-order shape of the ejecta cloud but not influencing the basic cant angle discussed in the main text. These approximations all require that the velocity change is much smaller than the orbital velocity.

the denominator of Equation S3, and also using Equation S2, the cant angle for this case θ_2 is expressed as[5]

$$\tan\theta_2 = \frac{\Delta r}{a\Delta\lambda} = \frac{\Delta a - ae\cos\Omega t}{\frac{3}{2}\Delta a\Omega t - 2ae\sin\Omega t}. \tag{S5}$$

Since $e \sim |\Delta a|/a$ as noted above, and resolving the sign ambiguity by noting that particles with $\Delta a > 0$ start at periapse while those with $\Delta a < 0$ start at apoapse, this becomes

$$\tan\theta_2 = \frac{1 - \cos\Omega t}{\frac{3}{2}\Omega t - 2\sin\Omega t}. \tag{S6}$$

This curve, which is plotted as the solid line in Figure S6a, is identical to the cant angles derived in analytical and numerical calculations involving realistic distributions of ejecta velocities (*29*). Qualitatively, the cant angle passes through zero (horizontal) whenever the number of orbits elapsed since impact is an integer, while bouncing up to a maximum value between such times; furthermore, the amplitude of the bounce (i.e., the maximum cant angle reached when the number of orbits elapsed since impact is an integer plus a half) decays with time in a fashion similar to Equation S4.

The ejecta cloud in the A ring was observed on two occasions separated by about a day, which are designated as “Ax(1)” and “Ax(2)” in Table S2. The radius-longitude locations of the two apparitions are consistent with them being the same structure. The radii are equal to within the error bars, and the difference in the inertial longitudes is $-49.5° \pm 0.2°$, which can be compared with the keplerian mean motion at that location ($\Omega = 656.89°$ day^{-1}) accumulated over the elapsed time between the images (88,168 seconds, see Table S1). The latter is $\Omega t = 670.33°$, which is equivalent to the completion of 2 full orbits plus a longitude offset of $-49.67°$, consistent with the observed difference within the error bar. In Figure S6a, the horizontal gray bars indicate the two measured values of the cant angle for the two apparitions in the A ring, with

---

[5] Instead of $\cos\Omega t$ and $\sin\Omega t$, a strictly correct version of Equation S5 would include $\cos\kappa t$ and $\sin\kappa t$, where the time between periapses $2\pi/\kappa$ is not identical to the orbit period $2\pi/\Omega$ due to precession. However, we ignore this effect, which amounts to a few percent difference in the residuals.

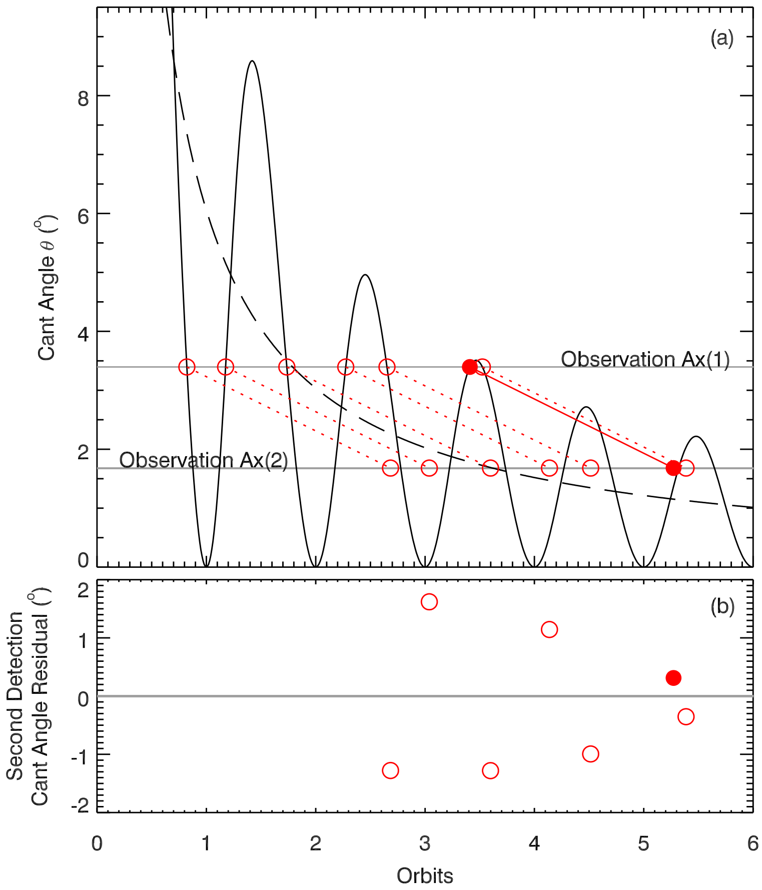

Figure S6: (a) The cant angle of the ejecta cloud as a function of time elapsed since the initial cloud-creating impact, as expected from (dashed line) simple keplerian shear resulting from an initially distributed ejecta cloud and from (solid line) a realistic model starting with ejecta at a single point (impact site) with a distribution of velocities. The two horizontal gray bars indicate the two measured values of the cant angle; additionally, the horizontal distance between each pair of red circles is fixed by the time elapsed between the two measurements, so the line connecting each pair has a fixed length and orientation. However, the assemblage can slide horizontally because the time of the initial impact is not directly known. The upper set of red circles mark the 7 locations at which the solid curve passes through the first cant angle measurement (3.40°), and the lower set of red circles marks the consequent time for the second measurement (1.68°). (b) Residuals between the lower set of red circles and the solid line. The best solution, for which the circles are filled, places the two observations at, respectively, 3.4 and 5.3 orbital periods after the initial impact. A much better solution is shown in Figure S7.

their thicknesses indicating the uncertainties. For each pair of plotted red circles, the connecting line has a known length and orientation, since the time elapsed *between the observations* is also known. What is not known is the time of the initial impact (creation of the cloud), which means that the pair of plotted circles can slide in the horizontal direction, looking for a location at which both circles fall as closely as possible on the solid curve.

As the time at which the images were taken is known very precisely, the primary source of uncertainty in the horizontal coordinate is in the mean motion used to convert the elapsed time from seconds to number of orbits. Since the observed clouds extend over a radial range, the mean motion could vary by as much as 0.3%, but this introduces only negligible changes in the residuals described below, so we will not consider it further.

3.1 Isotropic ejecta from a single impactor

There are 7 locations at which the solid curve passes through the first cant angle measurement (3.46°), and these are marked by the upper set of red circles in Figure S6a. For each of these, there is a consequent time for the second cant angle measurement (1.63°), which are marked by the lower set of red circles. A plausible solution for the initial impact time is one for which the latter circle also falls on the solid curve. The residuals are plotted in Figure S6b, where it is seen that the candidate solutions for which the impact ($t = 0$) is recent with respect to the first observation all have very large residuals. The sixth candidate solution (shown with filled circles in Figure S6) has the smallest residual at 0.31°, or more than 18σ. Furthermore, this solution would indicate that the first apparition occurred when the cloud was more than 3 orbits old, which is not a preferred solution since, as discussed below, the ejecta cloud should fade with time and thus the observed cloud brightness would imply a much larger initial impact.

3.2 Directed ejecta from a single impactor

Equation S6 holds when the ejecta velocities are isotropic. However, an impactor arriving from a certain direction may result in an initially directed ejecta cloud. In such a case, if the ejecta is directed at an angle ϕ from the azimuthal direction, the cant angle becomes

$$\tan\theta_3 = \frac{\cos\phi(1-\cos\Omega t) - \frac{1}{2}\sin\phi\sin\Omega t}{\cos\phi(\frac{3}{2}\Omega t - 2\sin\Omega t) - \sin\phi(1-\cos\Omega t)}. \tag{S7}$$

Note that this reduces to Equation S6 when $\phi = 0$.

Although, in principle, a directed ejecta cloud governed by Equation S7 opens up more parameter space in which a match to our data might be found, in practice this exercise turned out to be unfruitful. No improved residuals were found for any value of ϕ; furthermore, ejection near the radial direction ($\phi \sim 90^\circ$) results in some cant angles that are very large and others that are less than zero, neither of which appears in our observations. Thus, the idea of a directed ejecta cloud does not appear to alleviate the difficulties discussed in the previous section.

3.3 Ejecta from a distributed stream of impactors

Returning to what we initially thought was too simplistic an assumption, we note that an ejecta cloud evolving under simple keplerian shear (see Equation S4 and the dashed line in Figure S6) gives quite a good residual of 0.016°. This is 0.9σ, an excellent agreement and twenty times better than the best candidate in Section 3.1, despite only one candidate location at which the data cross the evolution curve (Figure S7).

The most likely physical mechanism for an ejecta cloud evolving under simple keplerian shear, which requires ejecta particles to have roughly circular orbits with semimajor axes that are offset from one another, is that the impactor was a cloud or stream of particles, rather than a single object. Such a stream of particles might readily form along the trajectory of a cometary body, and essentially the same phenomenon was recently hypothesized by (*17*) as the trigger

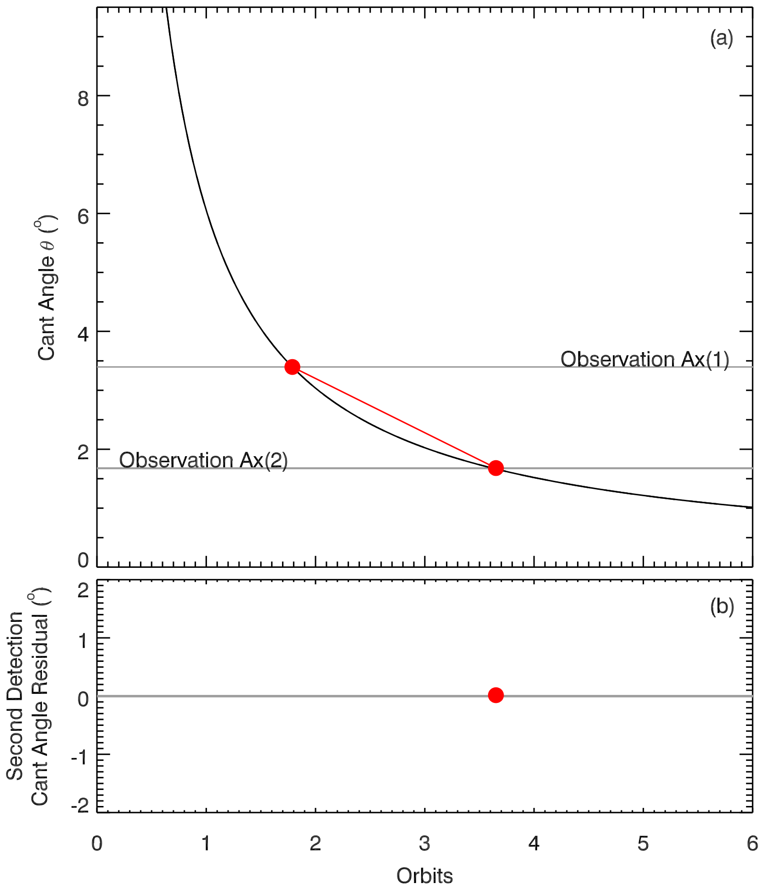

Figure S7: (a) The cant angle of the ejecta cloud as a function of time elapsed since the initial cloud-creating impact, as expected from simple keplerian shear resulting from an initially distributed ejecta cloud. The red circles, red solid line, and horizontal gray bars are as in Figure S6. In this case, the solid curve passes through the first cant angle measurement at only one location (1.8 orbital periods after the initial impact), resulting in only one candidate consequent time for the second measurement (3.6 orbital periods after the initial impact). (b) The residual in this case is much better than for the best solution in Figure S6.

for a slight tilting of the C and D rings that evolved into an observed corrugated pattern. In both cases, the stream of impactors has been invoked because observations are consistent with ring particles over a large region having been perturbed in roughly the same way at the same time; however, the phenomenon proposed in this paper is on a much smaller scale.

The simplest scenario for creating a stream of impactors is for an interplanetary meteoroid to first suffer an impact with the ring that does not create much ejecta but which breaks up the meteoroid. The stream of material then completes a partial orbit of Saturn and suffers a second impact, producing the cloud that we have observed.

4 Ablation of ejecta cloud

The measured brightness (in terms of equivalent area) of the A-ring ejecta cloud decreased between the observations "Ax(1)" and "Ax(2)" (Table S3). The primary mechanism for ablation of the cloud is the fact that the initial vertical velocity component received by all ejecta particles, which is what allows them to rise above the ring plane and be seen, puts them on inclined orbits that must crash through the ring plane twice during every orbital period. As with the periapse directions discussed above, all ejecta particles will also have their nodal line (the intersection between a particle's orbit plane and the ring plane) more or less aligned with each other and with the initial impact site. Thus, the entire ejecta cloud will crash through the ring plane every half-orbit as elapsed from the initial impact time. Only very low-inclination ejecta trajectories will have the collision probability enhanced by their inclinations, since the ring optical depth is set primarily by the areal coverage of opaque self-gravity wakes (SGWs), and the spacing between wakes is large compared to their vertical height (*16, 30*). Thus we expect the cloud to be ablated at each pass through the ring by a factor $e^{-\tau}$, where τ is the ring optical depth, for a total ablation of $e^{-N\tau}$ where N is the number of times the cloud material has passed through the ring plane. Our observations of cloud brightness now allow us to measure the ring optical depth using

$$\tau = -\frac{1}{N} \ln \left(\frac{A_2}{A_1} \right), \tag{S8}$$

where A_1 and A_2 are the two measured equivalent areas. All of the solutions in Section 3.1 through 3.3 involve the occurrence of $N = 4$ ring-crossing events between the two observations. With the equivalent areas as reported in Table S3, we obtain $\tau = 0.65$. This closely matches the

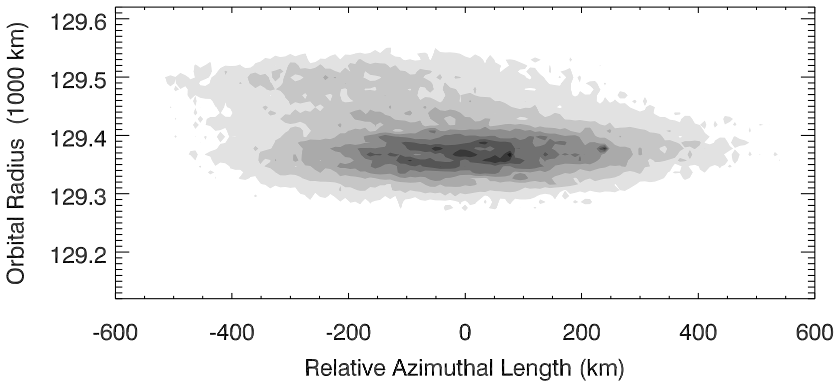

Figure S8: A contour plot showing feature "Ax(1)" (Figures 1 and S2) "rewound" to approximate its appearance immediately after the initial impact by shifting each row of the reprojected image left or right according to the fitted cant angle (Table S2).

actual optical depth of this region of the A ring, which is a combination of the areal coverage of opaque wakes and the optical depth of the gaps between the wakes (*16*).

5 Initial structure of feature "Ax"

The asymmetric structure of "Ax(1)" gives further information regarding the stream of impacting material that created it. We remove the effects of the cant angle by simply shifting each row of the reprojected image (Figure S2) by the amount given in Equation S3, effectively "rewinding" it to the moment of the cloud's creation, in order to better see aspects of its structure other than the cant angle. This representation, seen in Figure S8, yields two main insights.

The first insight is that the initial configuration of "Ax" has interesting radial structure, with a bright patch concentrated $\sim$100 km outward of the main part of the feature. It is also evident in Figures 1 and S2 that the outer portion of "Ax(1)" is brighter than the inner portion. This probably indicates that the impactor's initial velocity had a radially outward component, directing more ejecta in that direction.

The second insight is that the resulting approximation of the initial cloud is azimuthally elongated by a factor of $\sim$7. To be specific, the bright core of the feature is $\sim$100 km in the radial direction and $\sim$700 km in the azimuthal direction. This is consistent with an impactor stream centered around an eccentric and inclined Saturnian orbit with radial width $\sim$100 km at the location of intersection with the rings, if the time for the entire stream to pass through the ring was such that keplerian azimuthal motion of the target ring material was $\sim$600 km (the feature length minus the stream's cross-section diameter). That the orbit was Saturnian is indicated by the azimuthal alignment of the initial cloud as seen in Figure S8, indicating that the intersection between the impactor stream's orbit and the equatorial plane of Saturn remained stationary while the stream passed through the rings, which would occur naturally for a Saturnian orbit but would be highly unlikely for a heliocentric orbit. Since orbital speeds at a given distance from Saturn are roughly equal, even for objects on different orbits, this implies that the impactor stream was $\sim$600 km long.

Under this scenario, we can estimate the orbital parameters of the (fragments of the) projectile on the segment between the the two impacts on the rings, as well as the time elapsed in between. We assume without loss of generality that this is a keplerian trajectory with the ascending node intersecting the main rings (i.e., 80,000 km $< R_1 <$ 140,000 km) and the descending node at the "Ax" impact site ($R_2 =$ 129,350 km). Because individual particles of the stream have slightly different semi-major axes, say in the range Δa, they reach the impact site within a small time-span Δt. Employing Kepler's equation in the form $\Delta(nt) = \Delta n\, t + n\Delta t = 0$, we obtain the time elapsed between the initial disruption and the impact,

$$t = \frac{2}{3}\frac{a}{\Delta a}\,\Delta t. \tag{S9}$$

As discussed above, we use $\Delta a = 100$ km and Δt equal to 600 km multiplied by the keplerian velocity at impact, such that $\Delta t \approx 35$ seconds. The first-order estimate $a = R_2$ yields $t = 8.4$ hr. A refined estimate is obtained by using the conic section equation and the Kepler equation, together with Equation S9, yielding a closed set of transcendental equations that determine semi-major axis, eccentricity, and longitude of pericenter for each value of the radial location of the initial disruption R_1. We find a semi-major axis in the range 114,000 km $< a <$ 139,000 km, an eccentricity in the range $0.18 < e < 0.36$, a post-disruption velocity in the range 16 km s^{-1} $<$ $v_{\rm post}$ $<$ 25 km s^{-1} (70% to 80% of the incoming parabolic velocity $v_{\rm init}$), and the time elapsed between the two impacts in the range 7.4 hr $< t <$ 9.0 hr.

6 Multiple cant angles of feature "Cx"

As described in Section 2, the peripheral regions of feature "Cx" appear to have a steeper cant angle than does the bright central region (Figure S9). The most straightforward interpretation of these steeper cant angles is that the peripheral regions are in fact younger (following Equation S4), formed by secondary impacts. The orbital period at this location is 6.6 hr, so the measured cant angles (Table S2) are consistent with the left-hand (outward/trailing) region and the right-hand (inward/leading) region each forming between four and six half-orbits after the bright central region.

This could conceivably be due to the disruption of a particularly large piece of ejecta or target, though the details are uncertain. Reasoning naïvely from the C ring optical depth of $\tau \sim 0.1$, the probability of an object passing through the ring plane five times without hitting anything is $e^{-5\tau} \approx 60\%$. This rough estimate of the probability may be diminished by the physical size of a cm-sized or dm-sized object, but that effect may be roughly canceled if only particles on the larger end of the C ring particle-size distribution are sufficient to cause disruption.

We may also consider the possibility that the cant angle of the central region of "Cx" is somehow spurious. As we will show in Section 9 and Figure S11bc, the large apparent age derived from the central region's cant angle leads to an initial cloud that, for certain values of q,

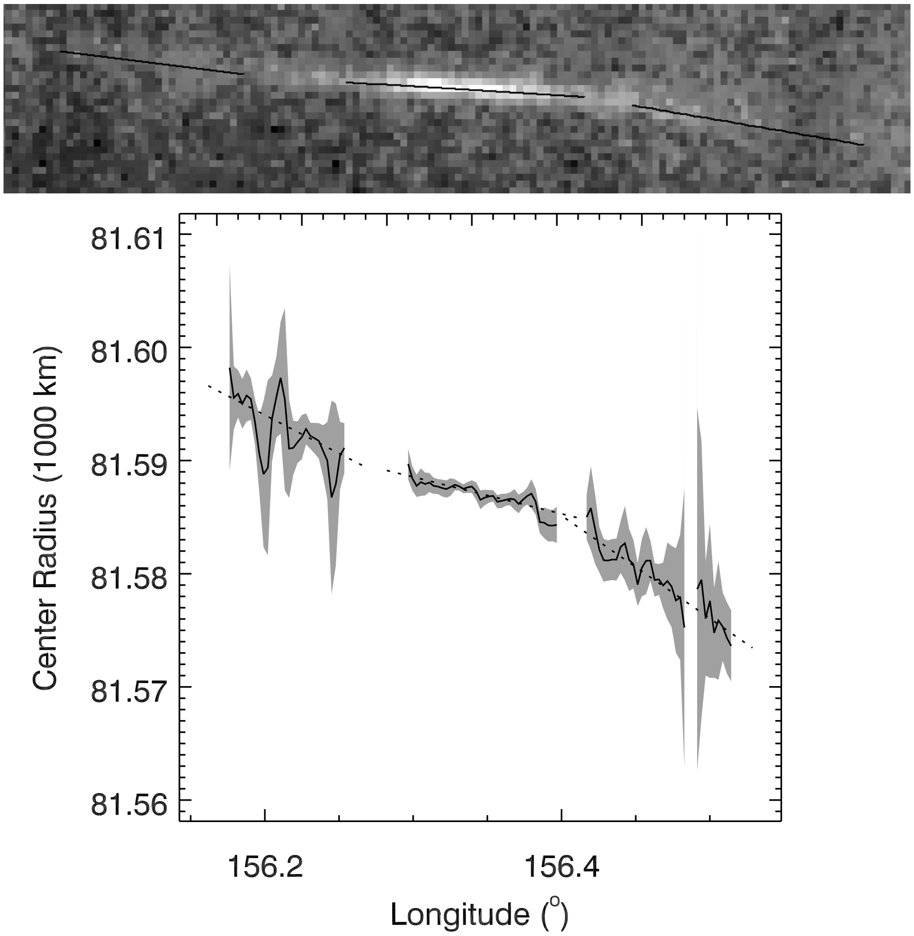

Figure S9: Larger, cropped versions of two panels of Figure S2, showing feature “Cx.” The reprojected image has the three fitted slopes overplotted.

is larger than the available target material.

7 Spectroscopy of feature “C6”

At very high phase angles, the broad color spectrum of a diffuse cloud is dominated by the different diffraction angles characteristic of each particle size (*31*). In the limiting case of a particle-size power-law index $q = 3$, every logarithmic particle-size bin contributes equal light-scattering area to the cloud, and the spectrum should be flat or “gray” (aside from any absorptions due to composition). For larger q, a prevalence of small particles causes the spectrum to be "bluish," while the opposite effect causes a "reddish" spectrum for smaller q (see, e.g., (*25*)). Since our observations of "C6" (Table S3) show a reddish color, which is to say that the integrated brightness (A) is nearly 2x as high in the infrared (wavelength $\lambda \sim 1\ \mu$m) as in the blue ($\lambda \sim 0.3\ \mu$m), this line of reasoning would lead us to infer a shallow size distribution with $q < 3$.

However, the assumption of a power-law size distribution may not be justified. The reddish color of spokes (*32*) has been attributed to a lack of μm-size particles due to a size cutoff (a higher value of $s_{\min}$, to use the terminology that will be introduced in Section 8), resulting in poor scattering of blue light. This may be due to substantial removal of small particles from the ejecta cloud, perhaps by electromagnetic effects.

It is also possible that some of the extra absorption seen at blue wavelengths may be due to composition rather than to particle size, comparable to the chemical absorptions at similar wavelengths inferred for Saturn's rings by VIMS (*33, 34*). Further detailed analysis is needed to understand the spectroscopy of "C6."

8 Mass of initial ejecta cloud

Again using the principle that the cloud is ablated by a factor $e^{-\tau}$ at every pass through the ring plane, we can estimate the equivalent area (all mentions of equivalent area in this section are A^{τ}, i.e., calculated in terms of optical depth) of the cloud "Ax" when it first formed, which is given by

$$A_{\text{initial}} = A_1 e^{N\tau}. \tag{S10}$$

Using the "Ax(1)" value from Table S3 as A_1, and $\tau = 0.65$ from Section 4, we have $A_{\text{initial}} =$ 26,000 km^2 (for $q = 3$; see Table S4). We use $N = 3$, which corresponds to the impactor-stream solution from Section 3.3 (see Figure S7), which we have already shown is preferable on the basis of residuals with the cant-angle model (Section 3.3), a younger and thus more likely age at first observation (cf. Section 3.1), and the initial horizontal orientation of the cloud "Ax" (Section 5). We will further show in Section 9 that the alternative solid-impactor solution from Section 3.1 (see Figure S6) has the additional difficulty of insufficient target material.

The equivalent area can be related to the number of particles by

$$A = \int_{s_{\min}}^{s_{\max}} \pi s^2 n(s) \mathrm{d}s, \tag{S11}$$

where $n(s)\mathrm{d}s$ is the number of particles with radius between s and $s + \mathrm{d}s$. We assume a truncated power-law size distribution, expressed by $n(s) = n_0 s^{-q}$, where the power-law index q is a real number, with sizes ranging from $s_{\min}$ to $s_{\max}$. We integrate to find

$$A = \begin{cases} \pi n_0 \ln\left(\frac{s_{\max}}{s_{\min}}\right) & \text{for } q = 3, \\ \frac{\pi n_0}{3-q}\left(s_{\max}^{3-q} - s_{\min}^{3-q}\right) & \text{otherwise.} \end{cases} \tag{S12}$$

We now turn to the mass of the cloud, which is given by

$$M_{\text{cloud}} = \int_{s_{\min}}^{s_{\max}} \frac{4}{3}\pi s^3 \rho_{\text{ejecta}} n(s) \mathrm{d}s, \tag{S13}$$

where we take the internal density of particles to be $\rho_{\text{ejecta}} = 0.9$ g cm^{-3}. Integrating this, we find

$$M_{\text{cloud}} = \begin{cases} \frac{4\pi\rho_{\text{ejecta}} n_0}{3} \ln\left(\frac{s_{\max}}{s_{\min}}\right) & \text{for } q = 4, \\ \frac{4\pi\rho_{\text{ejecta}} n_0}{3(4-q)}\left(s_{\max}^{4-q} - s_{\min}^{4-q}\right) & \text{otherwise.} \end{cases} \tag{S14}$$

Since $s_{\max} \gg s_{\min}$ (though this cannot be relied upon when their respective exponents approach zero), we can relate Equations S12 and S14 by

$$M_{\text{cloud}} = \begin{cases} \frac{4/3}{\ln(s_{\max}/s_{\min})} A \rho_{\text{ejecta}} s_{\max} & \text{for } q = 3, \\ \frac{4}{3}\ln\left(\frac{s_{\max}}{s_{\min}}\right) A \rho_{\text{ejecta}} s_{\min} & \text{for } q = 4, \\ \frac{4(3-q)}{3(4-q)} A \rho_{\text{ejecta}} \frac{\left(s_{\max}^{4-q} - s_{\min}^{4-q}\right)}{\left(s_{\max}^{3-q} - s_{\min}^{3-q}\right)} & \text{otherwise.} \end{cases} \tag{S15}$$

It is evident that the mass of the ejecta cloud, as constrained by its observed brightness, is highly dependent on the distribution of particle sizes within it (Figure S10). We will use

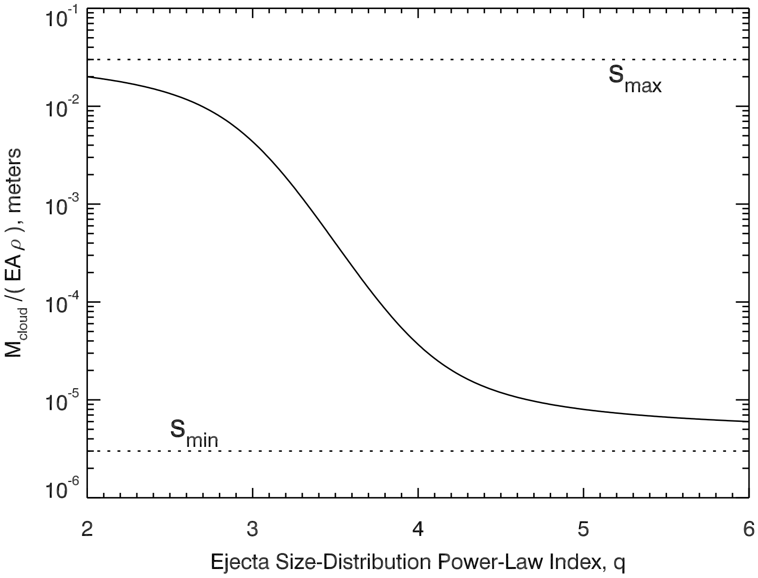

Figure S10: The ratio of cloud mass to the product of equivalent area and particle density (Equations S15), as a function of the size-distribution power-law index q. Note that the plotted ratio approaches $s_{\max}$ as q approaches zero, and approaches $s_{\min}$ as q approaches infinity, with a sharp transition in the range $3 < q < 4$. For this plot we used for $s_{\max} = 3$ cm and $s_{\min} = 3$ μm, but the curve's shape relative to $s_{\max}$ and $s_{\min}$ (the horizontal dotted lines) is generally applicable, with the transition becoming steeper when $s_{\max}$ and $s_{\min}$ are farther apart. Also note that, for mid-phase detections such as "Ax(1)" and "Ax(2)," the cloud mass depends even more strongly on q due to the effect described in Figure S4.

$s_{\min} \approx 3$ μm, following the spectroscopic analysis in Section 7. We will start with $q = 3$, the value for which each bin of constant $\mathrm{d}s$ contains equal mass and each bin of constant $\mathrm{d}\log s$ contains equal light-scattering area, but will allow q to vary as we progress with our analysis; $q = 3$ is a common result of fracturing, though the cloud could become enriched in small particles (raising q, or perhaps resulting in a particle-size distribution more complex than a single power law) if small particles are ejected at higher velocities and persist longer in the cloud or if small particles are preferentially produced by the impact mechanics (*35, 36*). We will also start with $s_{\max} = 3$ cm, though all we know is that $s_{\max}$ must be smaller than both the largest particles in the impactor stream and the largest target ring particles, and it could plausibly vary by several orders of magnitude.

9 Size of impactor

Given the initial ejecta cloud mass, we can infer the mass of the impactor by simply assuming a yield factor Y such that

$$M_{\text{initial cloud}} = Y M_{\text{impactor}}, \tag{S16}$$

For impacts onto icy surfaces, a common value is $Y \approx 10^4$ (see, e.g., (*1*)). Of course, this is a rough estimate at best, as the yield will depend on the dynamics of impacts onto a ring, which has not been investigated in detail. As guidance for future studies of impacts onto rings, we note that Saturn's A ring is pervaded by a clumpy microstructure called self-gravity wakes (SGWs), which arise due to the interplay between the ring's self-gravity and Saturn's tides (see, e.g., (*15, 37*)). For impactors larger than the Toomre critical wavelength,[6] impact is certain and the mass encountered is equal to the cross-section multiplied by the overall surface density σ. For impactors smaller than the Toomre critical wavelength, the transparency $T = e^{-\tau}$ is the probability that the impactor will encounter ring material at all; if it does impact, it will strike a mass equal to its cross-section multiplied by the SGW surface density σ_{SGW}, which may be comparable to σ/T (the enhancement factor $1/T$ is approximately half an order of magnitude). For impactors that are even smaller than the largest particles, there is some probability of striking an object bigger than the impactor. All three of these scenarios would result in differences in the impact mechanics, including in the primary ejecta direction.

Finally, the size of the impactor (prior to any breakup) is

$$R_{\text{impactor}} = \left(\frac{3M_{\text{impactor}}}{4\pi\rho_{\text{impactor}}} \right)^{1/3}. \tag{S17}$$

---

[6] The Toomre critical wavelength $\lambda_{\text{crit}} = 4\pi^2 G\sigma/\Omega^2$, where σ is the ring surface density and Ω is the local mean motion and G is Newton's constant, is the characteristic wavelength of SGWs (see, e.g., (*15, 37*)).

Here we note a final difficulty with the hypothesis that the observed cloud was created by a solid object impacting the rings, which is that the available target mass $M_{\mathrm{target}}^{\mathrm{solid\ impactor}} = \pi R_{\mathrm{impactor}}^2 \sigma$ is given by (combining Equations S16 and S17)

$$\frac{M_{\mathrm{target}}^{\mathrm{solid\ impactor}}}{M_{\mathrm{initial\ cloud}}} = \left(\frac{2.2 \times 10^{-6}\ \mathrm{kg}}{M_{\mathrm{initial\ cloud}}} \right)^{1/3} \tag{S18}$$

when we use $\sigma = 50$ g cm^{-2}, a standard value for the A ring (e.g., (*38*)). Since even the smallest clouds observed in this work have $M_{\mathrm{initial\ cloud}} \gtrsim 10^3$ kg (see Figure S11bc), a solid impactor simply will not encounter enough ring material to plausibly account for the observed ejecta clouds.[7] However, an impactor that has been broken up prior to impact does not have this problem because the available target mass is instead

$$M_{\mathrm{target}}^{\mathrm{impactor\ stream}} = \pi R_{\mathrm{stream}}^2 \sigma, \tag{S19}$$

which is 3×10^{12} kg for "Ax" (for which $R_{\mathrm{stream}} \approx 50$ km; see Figure S8) and is much larger than M_{cloud} (as, physically, it must be) for all observed features, with some dependence on model assumptions (Figure S11a).

In conclusion, given the strong dependence of the inferred cloud mass on q, the most we can say about the "Ax" impactor is that, before its preliminary break-up, it was between 1 m and 10 m in radius. On the other hand, the fact that plausible cloud masses are only obtained for certain values of q and s_{max} gives us new information on the characteristics of likely particle-size distributions of ejecta clouds from impacts onto rings. The most common result of fracturing, $q = 3$, is only possible for fairly low values of $s_{\mathrm{max}} \lesssim 3$ cm. For larger values of the upper size cutoff, we must have $q \gtrsim 3.5$. Of course, the particle-size distribution needn't be a power law in the first place, as we have thus far assumed it to be; more detailed modeling of ejecta from impacts onto rings is needed, and our results will provide useful constraints.

---

[7] Although it is conceivable that the observed cloud is composed mainly of material from the impactor, rather than material from the ring, this cannot be the case because then the ejecta would be distributed about the impactor's incoming orbit, rather than about the ring plane.

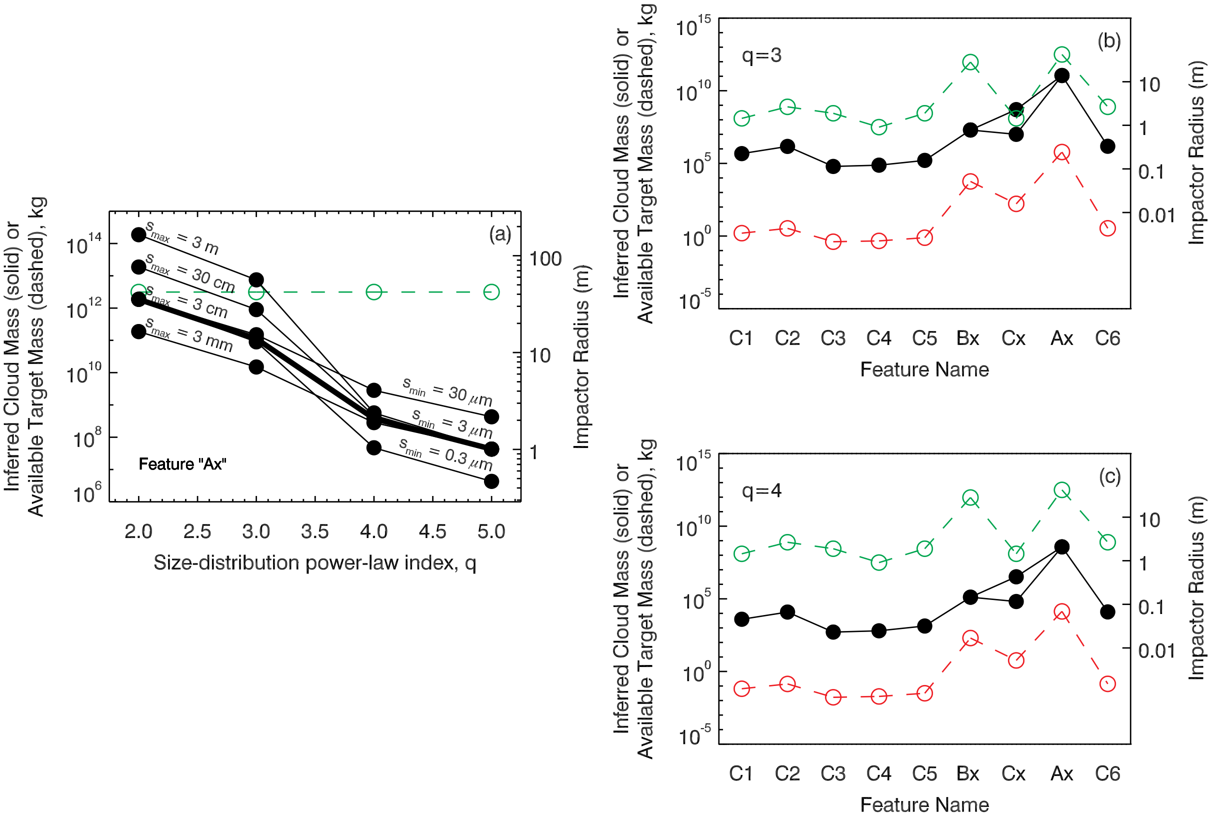

Figure S11: In all panels, solid black lines are the cloud mass $M_{\text{initial cloud}}$ inferred from observations as well as (using the right-hand axis) the radius of the inferred interplanetary impactor, the red dashed line is the available target mass for a solid impactor $M_{\text{target}}^{\text{solid impactor}}$ (Equation S18), and the dashed line is the available target mass for an impactor stream $M_{\text{target}}^{\text{impactor stream}}$ (Equation S19). (a) Values for feature "Ax" as a function of size-distribution power-law index q, plotted for various values of the minimum size cutoff s_{min} and the maximum size cutoff s_{max}. By Equation S15, s_{min} primarily affects the result for $q \gtrsim 4$ and s_{max} primarily affects the result for $q \lesssim 3$. The bold line denotes our favored solution, $s_{\text{min}} = 3\ \mu$m and $s_{\text{max}} = 3$ cm, for which the available target mass is larger than the inferred cloud mass for $q \gtrsim 3$. Larger values of s_{max}, however, would push the acceptable solutions to $q \gtrsim 3.5$. (b) Values for all observed features for $q = 3$. The higher of the two values for "Cx" is for the central region, while the lower is for the peripheral regions (see Table S3 and Section 6). Note that, for all features, $M_{\text{target}}^{\text{solid impactor}}$ is grossly insufficient to account for M_{cloud} while $M_{\text{target}}^{\text{impactor stream}}$ is sufficient except for the central region of "Cx." (c) The same as panel (b), but for $q = 4$. For this case, $M_{\text{target}}^{\text{impactor stream}}$ is sufficient for all features to account for M_{cloud}.

Using feature “Ax” as a verifying example, we can apply similar reasoning to the other observed features, all of which were observed only on one occasion and thus are without any verified information about their evolution (Figure S11bc).

10 Impactor Flux

Having estimated the masses of the impactors, we can say something about the abundance and size distribution of meteroids in the outer solar system, if we can estimate the frequency at which the observed events might be expected to occur. To estimate this, we combine the observed number of events with the area covered by images in which such events *could have been* observed.

Surprisingly, the two detections of “Ax” seem to be remarkable coincidence. The sequences of images that detected “Ax(1)” and “Ax(2)” only imaged 5% and 11% of the A ring, respec-

Table S5: Fractional area coverage of observations that detected ejecta clouds.

Image Range (Detected Features)	C ring	B ring	A ring
N1493791286–N1493792962 (C1–C5)	0.5%	0.0%	0.0%
N1628587518–N1628596780 (Bx)	13.9%	12.1%	9.3%
N1628666718–N1628684916 (Cx)	1.4%	0.0%	0.2%
N1628845250–N1628846513 (Ax(1))	0.0%	0.0%	5.2%
N1628920479–N1628943346 (Ax(2))	19.6%	15.5%	11.0%
N1721654739–N1721657155 (C6)	1.5%	0.0%	0.7%

Table S6: Parameters used to calculate the Estimated Influx Rate Φ shown in Figure 4.

Features	Orbit	Number	Areal Coverage[a]	Apparent Age[b]	Influx Rate[c]
C1–C5	007	5	4.8×10^{7}	1	2.9×10^{-17}
C1–C2	007	2	4.8×10^{7}	1	1.2×10^{-17}
C1	007	1	4.8×10^{7}	1	5.8×10^{-18}
Bx	116	1	2.0×10^{9}	4	3.4×10^{-20}
Cx (central)	116	1	1.3×10^{8}	30	7.2×10^{-20}
Cx (peripheral)	116	1	4.8×10^{7}	13	4.5×10^{-19}
Ax	116	1	1.8×10^{8}	23.5	6.6×10^{-20}
C6	169	1	1.4×10^{8}	0.86	2.3×10^{-18}
A (non-detection)	169	0	2.7×10^{7}	0.86	$< 1.2 \times 10^{-17}$

[a] In km^{2}; see Table S5.

[b] In hours; see Table S2.

[c] In m^{-2} s^{-1}; calculated as the number of detected features (or unity, in the case of an upper limit) divided by both the areal coverage and the apparent age.

tively, and the intersection between the two in co-rotating longitude (the area in which the feature appears) covers only 1% of the A ring at most. There was no retargeting between the two observations, nor any clear non-probabilistic reason why the large observed feature should appear in both image sequences. The non-detection of such a prominent feature in the 15% of the A ring that was imaged only in one or the other sequence of images demonstrates that the appearance of the feature in the 1% of the A ring that was imaged in both sequences of images does not reflect its true frequency.

Table S5 shows the fractional area coverage of each of the three main ring regions for each sequence of images that detected a feature described in this work. Although uncertainties are high due to the small number of detections, Figure 4 shows the inferred influx rate of meteoroids, calculated by dividing the number of features detected by each sequence of images by the areal coverage and by the inferred age of the feature. Consistent with previous investigators (*1*), we do not correct for Saturn's gravitational focusing, which would affect the results by a factor of a few at most.

The impactor radii in Figure 4 are calculated as part of the calculation that generated the values in Figure S11bc. The number of detected features is then normalized by the areal coverage of the sequence of images (Table S5) and by its estimated age (Table S2). For details, see Tables S6 and S7.

Table S7: Parameters used to calculate the Impactor Radius R_{imp} shown in Figure 4.

Features	Orbit	Minimum Initial Cloud Mass[a] ($M_{\mathrm{cloud}}^{q=3}$)	Minimum Impactor Radius[b] ($R_{\mathrm{imp}}^{q=3}$)	Minimum Initial Cloud Mass[a] ($M_{\mathrm{cloud}}^{q=4}$)	Minimum Impactor Radius[b] ($R_{\mathrm{imp}}^{q=4}$)
C1–C5	007	5.6×10^4	0.11	5.0×10^2	0.023
C1–C2	007	4.5×10^5	0.22	3.8×10^3	0.045
C1	007	1.5×10^6	0.33	1.2×10^4	0.065
Bx	116	2.0×10^7	0.78	1.4×10^5	0.15
Cx (central)	116	5.1×10^8	2.3	3.3×10^6	0.43
Cx (peripheral)	116	1.0×10^7	0.62	7.2×10^4	0.12
Ax	116	1.1×10^{11}	13.9	3.8×10^8	2.1
C6	169	1.5×10^6	0.33	1.3×10^4	0.067
A (non-detection)	169	1.5×10^6	0.33	1.3×10^4	0.067

[a] In kg; see Figure S11.

[b] In meters; calculated via Equations S16 and S17.

The five unambiguous data points in Figure 4 can be fit to a power law that matches well with previous understanding of interplanetary meteoroids while filling in a previously unprobed gap in the size distribution. We estimate the influx of meteoroids at 10 AU to be $\Phi \approx (3 \times 10^{-9}\ \mathrm{m}^{-2}\ \mathrm{s}^{-1}) R_{\mathrm{impactor}}^{-3.6}$ if $q = 3$ and $\Phi \approx (3 \times 10^{-10}\ \mathrm{m}^{-2}\ \mathrm{s}^{-1}) R_{\mathrm{impactor}}^{-3.6}$ if $q = 4$. This is broadly consistent with previous estimates of the interplantery meteoroid size spectrum at Saturn (*1, 8*), in that for some particle-size distributions (e.g., $q = 4$, $s_{\mathrm{min}} = 3\ \mu\mathrm{m}$, $s_{\mathrm{max}} = 3$ cm) they intersect at $\Phi \approx 10^{-15}\ \mathrm{m}^{-2}\ \mathrm{s}^{-1}$ when $R_{\mathrm{impactor}} = 1$ cm. But that represents the largest particle size considered by (*1, 8*), while we probe the meteoroid size distribution up to 1 m and beyond.

11 Spokes

Spokes are radial markings on the ring, likely composed of dust raised by a meteoroid impact and subsequently affected by Saturn's magnetic field (*4, 5*). They occur in the central B ring, inward and slightly outward of 112,300 km, the "synchronous orbit" at which the period of a keplerian orbit matches the rotation rate of the planet and its magnetic field.

No ejecta clouds were observed in the region dominated by spokes, though our small number of observations means we can hardly rule out the possibility that a spoke-forming impact may also form an ejecta cloud. Under this hypothesis, ejecta clouds would be composed of larger particles that can persist for several orbital periods, while spokes are composed of dust particles small enough to acquire a significant charge-to-mass ratio and do not survive the ring-plane crossing after the first half-orbit (*5*). One ejecta cloud ("Bx") was observed in the B ring, but at 114,685 km (Table S2) it is several thousand km outward of the region from which spokes seem to grow, though the peripheries of a few spokes have been seen to reach outward as far as 115,000 km (*5*).

Spokes occur at a rate of approximately one per 15 degrees of ring longitude per hour (*21, 22*), which is $\Phi_{\mathrm{spoke}} \approx 4 \times 10^{-19}\ \mathrm{m}^{-2}\ \mathrm{s}^{-1}$. Using the meteoroid influx rates derived from our observations, as given in the previous section, this implies that the average size of the meteoroids that give rise to spokes is $R_{\rm impactor} = 50$ cm if our observed ejecta clouds have particle-size power-law exponent $q = 3$, or $R_{\rm impactor} = 10$ cm if $q = 4$.

References and Notes

1. J. N. Cuzzi, P. R. Estrada, Compositional evolution of Saturn's rings due to meteoroid bombardment. *Icarus* **132**, 1 (1998). doi:10.1006/icar.1997.5863

2. R. H. Durisen, P. W. Bode, J. N. Cuzzi, S. E. Cederbloom, B. W. Murphy, Ballistic transport in planetary ring systems due to particle erosion mechanisms. *Icarus* **100**, 364 (1992). doi:10.1016/0019-1035(92)90106-H

3. S. Charnoz, L. Dones, L. W. Esposito, P. R. Estrada, M. M. Hedman, in *Saturn from Cassini-Huygens*, M. Dougherty, L. Esposito, S. M. Krimigis, Eds. (Springer-Verlag, Dordrecht, Netherlands, 2009), pp. 537–575.

4. C. K. Goertz, G. Morfill, A model for the formation of spokes in Saturn's ring. *Icarus* **53**, 219 (1983). doi:10.1016/0019-1035(83)90143-4

5. C. Mitchell, C. Porco, L. Dones, J. Spitale, The behavior of spokes in Saturn's B ring. *Icarus* 10.1016/j.icarus.2013.02.011 (2013).

6. M. R. Showalter, Detection of centimeter-sized meteoroid impact events in Saturn's F ring. *Science* **282**, 1099 (1998). doi:10.1126/science.282.5391.1099 Medline

7. R. S. French *et al.*, The brightening of Saturn's F ring. *Icarus* **219**, 181 (2012). doi:10.1016/j.icarus.2012.02.020

8. E. Grün, H. A. Zook, H. Fechtig, R. H. Giese, Collisional balance of the meteoritic complex. *Icarus* **62**, 244 (1985). doi:10.1016/0019-1035(85)90121-6

9. S. Bouley *et al.*, Power and duration of impact flashes on the Moon: Implication for the cause of radiation. *Icarus* **218**, 115 (2012). doi:10.1016/j.icarus.2011.11.028

10. L. S. Chambers, J. N. Cuzzi, E. Asphaug, J. Colwell, S. Sugita, Hydrodynamical and radiative transfer modeling of meteoroid impacts into Saturn's rings. *Icarus* **194**, 623 (2008). doi:10.1016/j.icarus.2007.11.017

11. Some "flashes" of unknown provenance were reportedly seen in Voyager data (*23, 24*), but these have not been confirmed nor generally accepted.

12. C. C. Porco *et al.*, Cassini imaging science: Instrument characteristics and anticipated scientific investigations at Saturn. *Space Sci. Rev.* **115**, 363 (2004). doi:10.1007/s11214-004-1456-7

13. Details of our observations and data reduction are given in sections 1 and 2 (respectively) of the supplementary materials (SM) text.

14. A. Van Helden, *Saturn*, in T. Gehrels, M. S. Matthews, Eds. (Univ. of Arizona Press, Tucson, AZ, 1984), pp. 23–43.

15. M. S. Tiscareno, in *Planets, Stars, and Stellar Systems, Volume 3: Solar and Stellar Planetary Systems*, T. D. Oswalt, L. French, P. Kalas, Eds. (Springer, Dordrecht, Netherlands, in press); http://arxiv.org/abs/1112.3305.

16. P. D. Nicholson, M. M. Hedman, Self-gravity wake parameters in Saturn's A and B rings. *Icarus* **206**, 410 (2010). doi:10.1016/j.icarus.2009.07.028

17. M. M. Hedman, J. A. Burns, M. W. Evans, M. S. Tiscareno, C. C. Porco, Saturn's curiously corrugated C ring. *Science* **332**, 708 (2011). doi:10.1126/science.1202238 Medline

18. All measured brightnesses are relative to the ring background.

19. J. E. Colwell *et al.*, in *Saturn from Cassini-Huygens*, M. Dougherty, L. Esposito, S. M. Krimigis, Eds. (Springer-Verlag, Dordrecht, Netherlands, 2009), pp. 375–412.

20. A. R. Poppe, M. Horányi, *Geophys. Res. Lett.* **39**, 15104 (2012).

21. J. N. Cuzzi, R. H. Durisen, Bombardment of planetary rings by meteoroids: General formulation and effects of Oort cloud projectiles. *Icarus* **84**, 467 (1990). doi:10.1016/0019-1035(90)90049-F

22. E. Grün, G. W. Garneau, R. J. Terrile, T. V. Johnson, G. E. Morfill, Kinematics of Saturn's spokes. *Adv. Space Res.* **4**, 143 (1984). doi:10.1016/0273-1177(84)90019-X

23. A. F. Cook, T. C. Duxbury, A fireball in Jupiter's atmosphere. *J. Geophys. Res.* **86**, 8815 (1981). doi:10.1029/JA086iA10p08815

24. A. F. Cook, R. Barrey, G. E. Hunt, *Bull. Am. Astron. Soc.* **15**, 814 (1983).

25. M. M. Hedman *et al.*, Spectral observations of the Enceladus plume with Cassini-VIMS. *Astrophys. J.* **693**, 1749 (2009). doi:10.1088/0004-637X/693/2/1749

26. J. N. Cuzzi *et al.*, in *Planetary Rings*, R. Greenberg, A. Brahic, Eds. (Univ. Arizona Press, Tucson, 1984), pp. 73-199.

27. M. R. Showalter, J. B. Pollack, M. E. Ockert, L. R. Doyle, J. B. Dalton, A photometric study of Saturn's Ring. *Icarus* **100**, 394 (1992). doi:10.1016/0019-1035(92)90107-I

28. B. R. Scharringhausen, A photometric model of the inclined F ring of Saturn, thesis, Cornell University (2007).

29. J. Schmidt, M. S. Tiscareno, F. Spahn, M. Seiß, *AAS Division for Planetary Sciences Meeting Abstracts* **43**, P159 (2011).

30. J. E. Colwell, L. W. Esposito, M. Sremčević, G. R. Stewart, W. E. McClintock, Self-gravity wakes and radial structure of Saturn's B ring. *Icarus* **190**, 127 (2007). doi:10.1016/j.icarus.2007.03.018

31. M. R. Showalter, J. A. Burns, J. N. Cuzzi, J. B. Pollack, Jupiter's ring system: New results on structure and particle properties. *Icarus* **69**, 458 (1987). doi:10.1016/0019-1035(87)90018-2

32. E. D'Aversa *et al.*, *Geophys. Res. Lett.* **37**, 1203 (2010).

33. J. Cuzzi *et al.*, in *Saturn from Cassini-Huygens*, M. Dougherty, L. Esposito, S. M. Krimigis, Eds. (Springer-Verlag, Dordrecht, Netherlands, 2009), pp. 459–509.

34. R. N. Clark *et al.*, The surface composition of Iapetus: Mapping results from Cassini VIMS. *Icarus* **218**, 831 (2012). doi:10.1016/j.icarus.2012.01.008

35. P. Michel, W. Benz, D. C. Richardson, Disruption of fragmented parent bodies as the origin of asteroid families. *Nature* **421**, 608 (2003). doi:10.1038/nature01364 Medline

36. D. D. Durda *et al.*, Size–frequency distributions of fragments from SPH/N-body simulations of asteroid impacts: Comparison with observed asteroid families. *Icarus* **186**, 498 (2007). doi:10.1016/j.icarus.2006.09.013

37. J. Schmidt, K. Ohtsuki, N. Rappaport, H. Salo, F. Spahn, in *Saturn from Cassini-Huygens*, M. Dougherty, L. Esposito, S. M. Krimigis, Eds. (Springer-Verlag, Dordrecht, Netherlands, 2009), pp. 413–458.

38. M. S. Tiscareno, J. A. Burns, P. D. Nicholson, M. M. Hedman, C. C. Porco, Cassini imaging of Saturn's rings. *Icarus* **189**, 14 (2007). doi:10.1016/j.icarus.2006.12.025